

Communication

# Incorporation of Iron(II) and (III) in Hydroxyapatite—A Theoretical Study

Olga Nikolaevna Makshakova <sup>1</sup>, Daria Vladimirovna Shurtakova <sup>2,\*</sup>, Alexey Vladimirovich Vakhin <sup>2</sup>, Peter Olegovich Grishin <sup>3</sup> and Marat Revgerovich Gafurov <sup>2</sup> 

<sup>1</sup> Kazan Institute of Biochemistry and Biophysics, FRC Kazan Scientific Center of Russian Academy of Sciences, 420111 Kazan, Russia; olga.makshakova@kibb.knc.ru

<sup>2</sup> Institute of Physics, Kazan Federal University, 18 Kremlevskaya Str., 420008 Kazan, Russia; vakhin-a\_v@mail.ru (A.V.V.); marat.gafurov@kpfu.ru (M.R.G.)

<sup>3</sup> Dentistry Faculty, Kazan State Medical University, 49 Butlerova Str., 420012 Kazan, Russia; phlus8@mail.ru

\* Correspondence: darja-shurtakva@mail.ru

**Abstract:** Hydroxyapatite ( $\text{Ca}_{10}(\text{PO}_4)_6(\text{OH})_2$ , HAp) doped with various transition metals has generated great interest in view of its potential application in a wide variety of fields, including in catalysis as a support with a series of attractive properties. Despite a large number of experimental works devoted to the synthesis and application of iron-substituted hydroxyapatites, problems concerning the location, introduced defects, and charge compensation schemes for  $\text{Fe}^{2+}$  and/or  $\text{Fe}^{3+}$  cations in the crystal structure of HAp remain unclear. This paper is devoted to the comprehensive analysis of iron (II) and (III) introduction into the HAp lattice by density functional theory (DFT) calculations. We show that the inclusion of  $\text{Fe}^{2+}$  in the Ca(1) and Ca(2) positions of HAp is energetically comparable. For the  $\text{Fe}^{3+}$ , there is a clear preference to be included in the Ca(2) position. The inclusion of iron results in cell contraction, which is more pronounced in the case of  $\text{Fe}^{3+}$ . In addition,  $\text{Fe}^{3+}$  may form a shorter linkage to oxygen atoms. The incorporation of both  $\text{Fe}^{2+}$  and  $\text{Fe}^{3+}$  leads to notable local reorganization in the HAp cell.

**Keywords:** calcium phosphate; hydroxyapatite; density functional theory; iron



**Citation:** Makshakova, O.N.; Shurtakova, D.V.; Vakhin, A.V.; Grishin, P.O.; Gafurov, M.R. Incorporation of Iron(II) and (III) in Hydroxyapatite—A Theoretical Study. *Crystals* **2021**, *11*, 1219. <https://doi.org/10.3390/cryst11101219>

Academic Editors: Réka Barabás, Liliana Bizo and Graziella-Liana Turdean

Received: 15 September 2021  
Accepted: 7 October 2021  
Published: 9 October 2021

**Publisher's Note:** MDPI stays neutral with regard to jurisdictional claims in published maps and institutional affiliations.



**Copyright:** © 2021 by the authors. Licensee MDPI, Basel, Switzerland. This article is an open access article distributed under the terms and conditions of the Creative Commons Attribution (CC BY) license (<https://creativecommons.org/licenses/by/4.0/>).

## 1. Introduction

Transition metal catalysts are of particular interest in a wide variety of fields. They are used in pharmaceuticals, in the production of natural products, chemistry, the hydrogenation of aromatic hydrocarbons, etc. An essential property of such catalysts is environmental friendliness and the possibility of repeated use. Metals such as rhodium, palladium, ruthenium, copper, and nickel are most commonly used as transition catalyst metals. Recently, iron has been added to this list [1–3]. The development of new catalytic systems with iron that meet environmental friendliness, efficiency, and reuse is a modern trend.

Iron compounds are widely used in catalysis in a heterogeneous and homogeneous form. For example, in alkylation reactions, iron compounds are highly active and can be superior in efficiency to catalysts based on other metals. The radical cation mechanism of benzylation with the intermediate formation of  $\text{Fe}^{2+}$  has been proposed for iron chloride supported on aluminum oxide [4]. The critical role of the simultaneous presence and ratio of  $\text{Fe}^{3+}/\text{Fe}^{2+}$  ions in ensuring the activity of iron-containing alkylation catalysts is shown in ref. [5]. Catalysts based on  $\gamma\text{-Fe}_2\text{O}_3$  nanoparticles supported on silicas have proven to be effective catalysts for many chlorolefin conversions, including isomerization of allyl chloro-olefins and alkylation of benzene with allyl chloride and benzyl chloride [6].

Iron oxides are widely used as catalysts in Fischer–Tropsch reactions, dehydrogenation, alkylation and other processes. They are also active in catalytic reactions with the participation of halogenated hydrocarbons, in which the catalytic properties of bulk and nanosized iron oxides differ significantly [7,8]. Iron-containing oxide catalysts are highly effective in

hydrogenation reactions of highly condensed organic matter [9] and aquathermolysis of heavy oil [10,11].

Hydroxyapatite ( $\text{Ca}_{10}(\text{PO}_4)_6(\text{OH})_2$ , HAp) is an attractive material for use in various fields, including catalysis applications [1–3,12–15]. Hydroxyapatite is a material well-known for cationic and anionic substitutions [16,17]. In the crystalline cell, calcium ions adopt two types of positions with different coordination. In the Ca(1) position, six oxygen atoms belonging to four orthophosphates are coordinated with one calcium ion (Figure 1). It forms  $\text{CaO}_6$  prism geometry, a polyhedron intermediate between an octahedron and a trigonal prism. In position Ca(2), calcium ion has seven oxygen atoms in the first coordination shell; six of them are from four orthophosphate groups and one from a hydroxyl. It forms a  $\text{CaO}_7$  distorted pentagonal bipyramid.

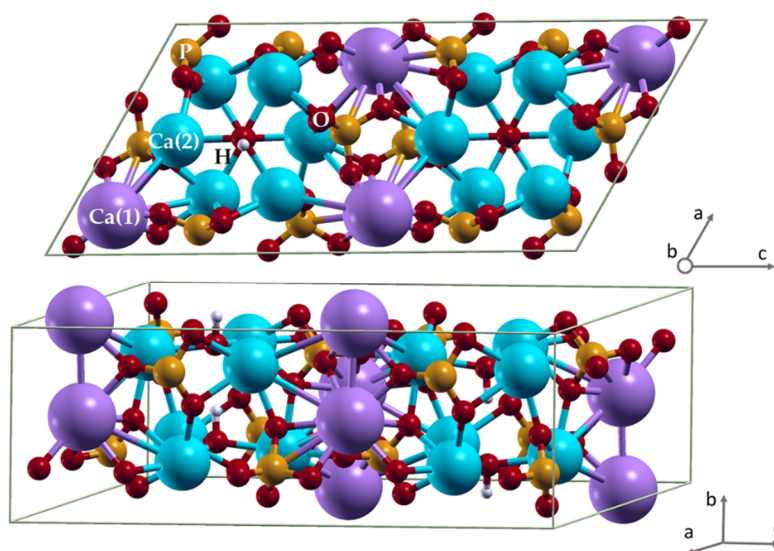


**Figure 1.** Hydroxyapatite unit cell. Color coding: phosphorus—orange, oxygen—red, hydrogen—light grey, Ca(1)—purple, Ca(2)—blue.

The adsorption capacity, high ion exchange capacity, lack of structural porosity, and low surface acidity are important properties of HAp when used as a catalyst [18,19]. The transition from micro-sized particles to nano-sized ones makes it possible to increase the external surface area and the number of catalytically active centers, and reduce the restrictions on mass transfer, thereby augmenting the catalytic activity [1]. Additionally, the cooperative catalytic effect between the active metal species of the HAp structure and the exchanges species, which are integrated into the HAp structure and immobilized on the surface, was noticed and explained in ref. [20], thereby making exchanged HAp efficient catalytic systems. Accordingly, the synthesis and study of HAp-based catalytic systems with iron impurities have attracted great interest in recent years [21–26].

As reviewed by Goldberg et al. [27,28], Fe-HAp and Fe oxide nanoparticles demonstrated high efficiency as a catalyst in the field of heavy oil purification via oxidative desulfurization and aquathermolysis methods, oil asphaltene extraction, etc. Besides catalytic applications, Fe-HAp nanoparticles are promising for cancer monitoring [29], as well as magnetic resonance imaging [30], targeted delivery of drugs, and for the treatment of cancer by a hyperthermic method [31].

It is a fact that the replacement of calcium with iron ions in the crystal structure affects its physicochemical properties [32]. The introduction of  $\text{Fe}^{3+}$  improves bactericidal and mineralizing properties of nanosized HAp [33]. Iron has a positive impact on osteoblast-like behavior [34]. The effect of iron ions on structural changes in HAp is reported by Morrissey et al. [35]. The effect of heat treatment and the concentration of iron oxide on the microhardness of HAp was described in the work of Filho et al. [36]. The paramagnetic properties of HAp appear upon the addition of  $\text{Fe}^{3+}$  ions, and with an increase in the

concentration of iron ions, the magnetic susceptibility increases [37]. Goldberg et al. [27,28] demonstrated that  $\text{Fe}^{3+}$  introduction leads to an increase in surface area of nanohydroxyapatite particles, improving their catalytic properties for desulfurization of the model heavy oil.

Despite the large number of experimental works devoted to the synthesis and application of iron-substituted hydroxyapatites, the aspects of location-introduced defects and charge compensation schemes for  $\text{Fe}^{2+}$ – $\text{Fe}^{3+}$  cations in the crystal structure of HAp remain unclear. This paper is devoted to comprehensively analyzing iron (II) and (III) introduction into the HAp lattice by DFT calculations.

## 2. Methods

Density Functional Theory with the plane-wave basis and Vanderbilt ultrasoft pseudopotentials [38] were carried out using the Quantum ESPRESSO program [39]. The Perdew–Burke–Ernzerhof version of the generalized gradient approximation of the exchange–correlation functional (GGA-PBE) [38] was used. The use of PBE functional revealed the good agreement of the theoretical cell parameters with the experiment [40]. The kinetic energy cutoffs of 45 Ry for the smooth part of the electron wave functions and of 300 Ry for the augmented electron density were set up (in agreement with previously denoted [41]).

The unit cell parameters and initial geometry for HAp were taken from [42,43]. The present results have been calculated for a  $1 \times 1 \times 1$  monoclinic supercell, space group  $P2_1/m$  with 88 atoms in the cell, which was previously proven to be sufficient to reproduce spectra of doped HAp crystals [43]. Simulation of HAp within the  $P6_3/m$  space group (44 atoms per unit cell) leads to unphysical duplication of each OH group by the m-mirror. The crystal structure with antiparallel hydroxyl groups (to compensate the electric polarization) in a double unit cell compared to the original hexagonal structure is monoclinic with the  $P2_1/m$  space group [42,43]. The difference in the notations of principal axes for the hexagonal and monoclinic modifications should not lead to confusion.

Optimization of the geometry was performed in two steps: 1. the atomic positions were relaxed, keeping the cell parameter fixed, and 2. both the coordinates and cell dimensions were fully relaxed. The convergence condition on forces was  $10^{-3}$  Ry/Bohr. The Brillouin Zone integration was performed on a Monkhorst-Pack  $2 \times 2 \times 1$  k-point mesh [44].

## 3. Results

Due to the difference in the degree of ionization, ferrous cation ( $\text{Fe}^{2+}$ ) and ferric cation ( $\text{Fe}^{3+}$ ) demonstrate a distinguished influence on hydroxyapatite cell parameters and local ion reorganization upon inclusion.  $\text{Fe}^{2+}$  has six electrons in 3d orbital, but  $\text{Fe}^{3+}$  has only five. Such a variation results in their different capacity to interact with their surrounding and to be of different ionic radius. The latter is about 70 pm for the ferrous cation and about 60 pm for the ferric cation. The inclusion of one cation of each iron type into the monoclinic HAp supercell of 88 atoms in Ca(1) or Ca(2) position has been calculated. Overall, four types of positions can be occupied.

The introduction of cations in hydroxyapatite may occur at both the Ca(1) and Ca(2) position. Therefore, the inclusion of  $\text{Fe}^{2+}$ , which leads to the  $\text{Ca}_{9.5}\text{Fe}^{2+}_{0.5}(\text{PO}_4)_6(\text{OH})_2$  formula, may potentially occur at each of the two positions and does not require any additional charge compensation. In contrast, the substitution of  $\text{Ca}^{2+}$  by  $\text{Fe}^{3+}$ , leading to the  $\text{Ca}_{9.5}\text{Fe}^{3+}_{0.5}(\text{PO}_4)_6\text{O}_2\text{H}_{1.5}$  formula, is accompanied by element perturbation, which can be a vacancy formation in the  $\text{H}^+$  position or in the  $\text{Ca}^{2+}$  position (provided that two trivalent cations are included). The release of one  $\text{Ca}^{2+}$  on every two calcium ions substituted by the trivalent cations leads to a major local perturbation, as was shown for  $\text{Al}^{3+}$  doping [39]. Therefore, to diminish the influence of the charge compensation scheme on the cell contraction, the release of  $\text{H}^+$  from  $\text{OH}^-$  was considered to bring the overall charge of the system to zero. The  $\text{OH}^-$  are located within the anion channel, surrounded by calcium ions, and do not largely influence the overall packing and the density of the cell. A similar scheme of charge compensation has been previously considered in Refs [27,28,45].

The inclusion of  $\text{Fe}^{2+}$  into the HAp cell in the Ca(1) position results in the decrease in cell volume from  $1073.7 \text{ \AA}^3$  in pure HAp down to  $1060.7 \text{ \AA}^3$  in the iron substituted one. The significant contraction, by 0.7%, occurs along the  $a$  and  $c$  axes. Upon the inclusion of  $\text{Fe}^{2+}$  in the Ca(2) position, the cell contraction is less pronounced, and the cell volume reaches the value of  $1067.1 \text{ \AA}^3$ . These two types of substitution in terms of energy gain are pretty similar, and the difference is 0.2 eV in slight favor of iron inclusion in the Ca(2) position.

The inclusion of  $\text{Fe}^{3+}$  in the HAp cell gives more pronounced contraction of the cell than the  $\text{Fe}^{2+}$  inclusion, namely  $1060.2 \text{ \AA}^3$  and  $1064.7 \text{ \AA}^3$  in the Ca(1) and Ca(2) position, respectively (Table 1). Therefore, the density of the cell is larger in Ca(1),  $3.17 \text{ g/cm}^3$ , than in Ca(2),  $3.15 \text{ g/cm}^3$ . Interestingly, the inclusion of  $\text{Fe}^{3+}$  in the Ca(2) position occurs notably more favorable, by 1.03 eV, than in the Ca(1) position, which is distinct from the  $\text{Fe}^{2+}$  insertion. Such a favorability agrees with the short bond formation. When  $\text{Fe}^{3+}$  is located in the Ca(2) position, a short bond with the distance  $\text{Fe}^{3+}\text{-O}$  of  $1.803 \text{ \AA}$  is formed. Such a bond, as we previously reported, is of a partly covalent nature [27]. Coordination with other O atoms, closest to iron, occurs at distances of 2.068, 2.107, 2.24, and  $2.259 \text{ \AA}$ . To compare, the  $\text{Ca}^{2+}\text{-O}$  distances are within  $2.3\text{--}2.5 \text{ \AA}$ . The shift of  $\text{Fe}^{3+}$  in respect to the original position of  $\text{Ca}^{2+}$  is  $0.404 \text{ \AA}$ . The most pronounced shift of the oxygen atom from the anion channel is  $0.513 \text{ \AA}$ . Notably, the coordination at distances less than  $2.1 \text{ \AA}$  results in the P-O bond length change. The P-O bond interacting with  $\text{Fe}^{3+}$  becomes stretched up to  $1.594 \text{ \AA}$ , while the other three P-O bonds remained within  $1.55 \text{ \AA}$ , as in non-perturbed molecules, or shortened down to  $1.53 \text{ \AA}$ . Such stretching is less for  $\text{Fe}^{2+}$  incorporation, reaching  $1.581 \text{ \AA}$ . The shortest distance  $\text{Fe}^{2+}\text{-O}$  is  $1.980 \text{ \AA}$  (Table 1).

**Table 1.** Some calculated parameters of the HAp supercell for  $\text{Ca}_{9.5}\text{Fe}^{2+}_{0.5}(\text{PO}_4)_6(\text{OH})_2$  with ferrous cation ( $\text{Fe}^{2+}$ ) and  $\text{Ca}_{9.5}\text{Fe}^{3+}_{0.5}(\text{PO}_4)_6\text{O}_2\text{H}_{1.5}$  with ferric cation ( $\text{Fe}^{3+}$ ). The length of the Ca-O bonds is given for pure HAp.

Iron	Substitution	Energy, Ry	Cell Volume, $\text{\AA}^3$	Fe-O, $\text{\AA}$	Ca-O, $\text{\AA}$
$\text{Fe}^{2+}$	Ca(1)	−3514.79383	1060.7	2.347	2.386
				2.360	2.417
				2.389	2.444
				2.459	2.467
				2.523	2.499
$\text{Fe}^{2+}$	Ca(2)	−3514.80879	1067.1	2.743	2.595
				1.994	2.329
				2.042	2.354
				2.051	2.373
				2.216	2.405
$\text{Fe}^{3+}$	Ca(1)	−3513.64081	1067.1	2.814	2.595
				2.056	2.386
				2.058	2.417
				2.111	2.444
				2.124	2.467
$\text{Fe}^{3+}$	Ca(2)	−3513.7161776	1064.7	2.132	2.499
				2.132	2.595
				1.803	2.373
				2.107	2.595
				2.068	2.689
				2.240	2.329
				2.259	2.354
					2.405

Thus, the results of DFT calculations demonstrate that  $\text{Fe}^{3+}$  is more reactive in terms of interactions with surroundings, forming shorter contacts to oxygen atoms than  $\text{Fe}^{2+}$ . The inclusion of  $\text{Fe}^{3+}$  into the Ca(1) or Ca(2) positions results in more pronounced cell

contraction than what occurs upon  $\text{Fe}^{2+}$  inclusion. Strikingly,  $\text{Fe}^{3+}$  shows a clear preference to substitute Ca(2) than Ca(1) (Figure 2).

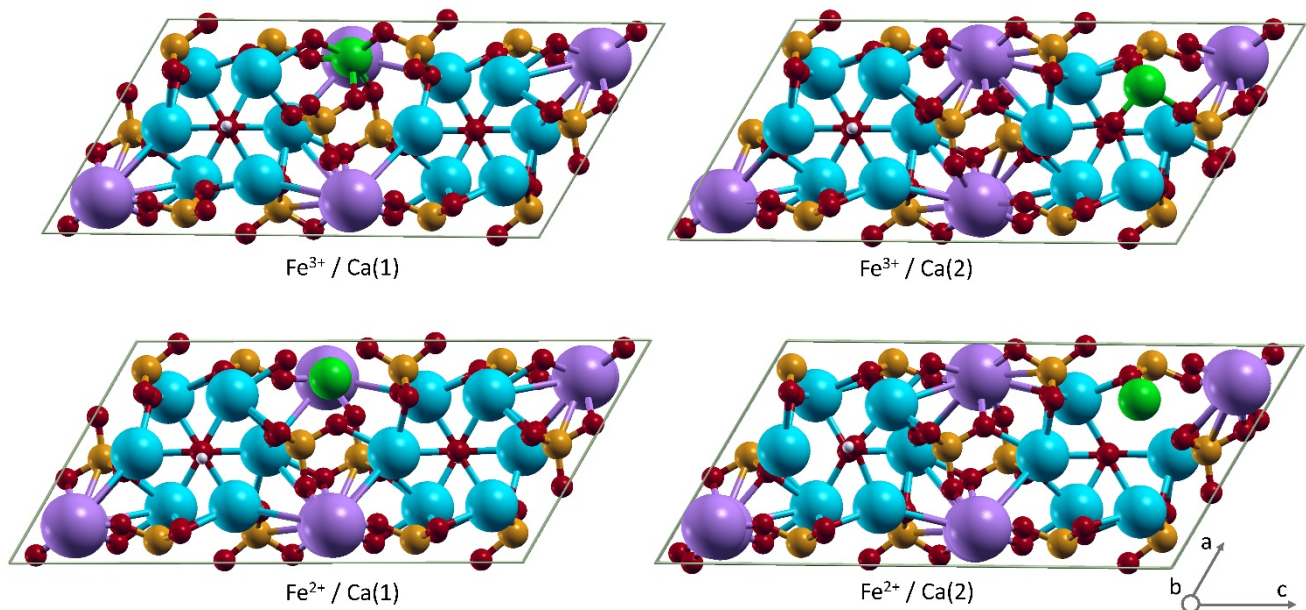


**Figure 2.** Hydroxyapatite unit cell with iron inclusion in Ca(1) and Ca(2) positions. Color coding: phosphorus—orange, oxygen—red, hydrogen—light grey, Ca(1)—purple, Ca(2)—blue, Fe—green.

#### 4. Conclusions

Since iron (III) inserted into the HAp matrix has been proven to be an efficient catalyst, it is vital to obtain details of its binding sites and interactions with its surrounding. Experimentally, it is challenging to provide an atomistic picture, since the iron impurity is distributed quite randomly over the HAp sample, and the mixture of positional states and population  $\text{Fe}^{2+}/\text{Fe}^{3+}$  can take place. These theoretical studies provide an indispensable tool to probe several isolated states to further compare with experimental data. In this work, we show that the inclusion of  $\text{Fe}^{2+}$  in the Ca(1) and Ca(2) positions is energetically comparable. For the  $\text{Fe}^{3+}$ , there is a clear preference to be included in the Ca(2) position. The inclusion of iron results in cell contraction, which is more pronounced in the case of  $\text{Fe}^{3+}$ . In addition,  $\text{Fe}^{3+}$  may form a shorter linkage to oxygen atoms. The incorporation of both  $\text{Fe}^{2+}$  and  $\text{Fe}^{3+}$  leads to significant local reorganization in the HAp cell. Furthermore, the ratio Ca(1)/Ca(2), which is 2/3 in pure HAp, varies upon iron inclusion, which may influence the catalytic properties of the complex material.

**Author Contributions:** Conceptualization, P.O.G. and M.R.G.; methodology, O.N.M.; validation, D.V.S.; investigation, O.N.M.; resources, A.V.V.; writing—original draft preparation, O.N.M., M.R.G., D.V.S.; writing—review and editing, D.V.S.; project administration, M.R.G.; funding acquisition, A.V.V. All authors have read and agreed to the published version of the manuscript.

**Funding:** This work was supported by the Ministry of Science and Higher Education of the Russian Federation under agreement № 075-15-2020-931 within the framework of the development program for a world-class Research Center “Efficient development of the global liquid hydrocarbon reserves”.

**Institutional Review Board Statement:** Not applicable.

**Informed Consent Statement:** Not applicable.

**Data Availability Statement:** Data can be available upon request from the authors.

**Conflicts of Interest:** The authors declare no conflict of interest.

## References

1. Zahmakıran, M.; Román-Leshkov, Y.; Zhang, Y. Rhodium (0) nanoparticles supported on nanocrystalline hydroxyapatite: Highly effective catalytic system for the solvent-free hydrogenation of aromatics at room temperature. *Langmuir* **2012**, *28*, 60–64. [[CrossRef](#)] [[PubMed](#)]
2. Vakh, C.; Kuzmin, A.; Sadetskaya, A.; Bogdanova, P.; Voznesenskiy, M.; Osmolovskaya, O.; Bulatov, A. Cobalt-doped hydroxyapatite nanoparticles as a new eco-friendly catalyst of luminol–H<sub>2</sub>O<sub>2</sub> based chemiluminescence reaction: Study of key factors, improvement the activity and analytical application. *Spectrochim. Acta Part A Mol. BioMol. Spectrosc.* **2020**, *237*, 118382. [[CrossRef](#)]
3. Gadipelly, C.; Deshmukh, G.; Mannepilli, L.K. Transition Metal Exchanged Hydroxyapatite/Fluorapatite Catalysts for C–C and C–N Bond Forming Reactions. *Chem. Rec.* **2021**, *21*, 1398–1416.
4. Salavati-Niasari, M.; Hasanalian, J.; Najafian, H. Alumina-supported FeCl<sub>3</sub>, MnCl<sub>2</sub>, CoCl<sub>2</sub>, NiCl<sub>2</sub>, CuCl<sub>2</sub>, and ZnCl<sub>2</sub> as catalysts for the benzylation of benzene by benzyl chloride. *J. Mol. Catal. A Chem.* **2004**, *209*, 209–214. [[CrossRef](#)]
5. Benaichouba, B.; Bussiere, P.; Vedrine, J.C. In-situ Mössbauer spectroscopic study of iron site evolution in iron and cobalt molybdates catalysts in propene oxidation reaction conditions. *Appl. Catal. A Gen.* **1995**, *130*, 31–45. [[CrossRef](#)]
6. Tsodikov, M.V.; Rostovshchikova, T.N.; Smirnov, V.V.; Kiseleva, O.I.; Maksimov, Y.V.; Suzdalev, I.P.; Ikorskii, V.N. Structure and size effects in Catal. by immobilized nanoclusters of iron oxides. *Catal. Today* **2005**, *105*, 634–640.
7. Hayashi, H.; Chen, L.Z.; Tago, T.; Kishida, M.; Wakabayashi, K. Catalytic properties of Fe/SiO<sub>2</sub> catalysts prepared using microemulsion for CO hydrogenation. *Appl. Catal. A Gen.* **2002**, *231*, 81–89. [[CrossRef](#)]
8. Kuhrs, C.; Arita, Y.; Weiss, W.; Ranke, W.; Schlögl, R. Understanding heterogeneous Catal. on an atomic scale: A combined surface science and reactivity investigation for the dehydrogenation of ethylbenzene over iron oxide catalysts. *Top. Catal.* **2000**, *14*, 111–123.
9. Derbyshire, F.; Hager, T. Coal liquefaction and catalysis. *Fuel* **1994**, *73*, 1087–1092. [[CrossRef](#)]
10. Aliev, F.A.; Mukhamatdinov, I.I.; Sitnov, S.A.; Ziganshina, M.R.; Onishchenko, Y.V.; Sharifullin, A.V.; Vakhin, A.V. In-Situ Heavy Oil Aquathermolysis in the Presence of Nanodispersed Catalysts Based on Transition Metals. *Processes* **2021**, *9*, 127. [[CrossRef](#)]
11. Lakhova, A.; Petrov, S.; Ibragimova, D.; Kayukova, G.; Safiulina, A.; Shinkarev, A.; Okekwe, R. Aquathermolysis of Heavy Oil Using Nano Oxides of Metals. *J. Pet. Sci. Eng.* **2017**, *153*, 385–390. [[CrossRef](#)]
12. Fihri, A.; Len, C.; Varma, R.S.; Solhy, A. Hydroxyapatite: A review of syntheses, structure and applications in heterogeneous catalysis. *Coord. Chem. Rev.* **2017**, *347*, 48–76. [[CrossRef](#)]
13. Pai, S.; Kini, S.M.; Selvaraj, R.; Pugazhendhi, A. A review on the synthesis of hydroxyapatite, its composites and adsorptive removal of pollutants from wastewater. *J. Water Process Eng.* **2020**, *38*, 101574. [[CrossRef](#)]
14. Ibrahim, M.; Labaki, M.; Giraudon, J.M.; Lamonier, J.F. Hydroxyapatite, a multifunctional material for air, water and soil pollution control: A review. *J. Hazard. Mater.* **2020**, *383*, 121139. [[CrossRef](#)] [[PubMed](#)]
15. Zhang, Y.; Li, Z.; Sun, W.; Xia, C. A Magnetically Recyclable Heterogeneous Catalyst: Cobalt Nano-Oxide Supported on Hydroxyapatite-Encapsulated  $\gamma$ -Fe<sub>2</sub>O<sub>3</sub> Nanocrystallites for Highly Efficient Olefin Oxidation with H<sub>2</sub>O<sub>2</sub>. *Catal. Commun.* **2008**, *10*, 237–242. [[CrossRef](#)]
16. Cacciotti, I. Cationic and anionic substitutions in hydroxyapatite. In *Handbook of Bioceramics and Biocomposites*; Antoniac, I.V., Ed.; Springer International Publishing: Bucharest, Romania, 2016; pp. 145–211. [[CrossRef](#)]
17. Zilm, M.E.; Chen, L.; Sharma, V.; McDannald, A.; Jain, M.; Ramprasad, R.; Wei, M. Hydroxyapatite substituted by transition metals: Experiment and theory. *Phys. Chem. Chem. Phys.* **2016**, *18*, 16457–16465. [[CrossRef](#)]
18. Tite, T.; Popa, A.C.; Balescu, L.M.; Bogdan, I.M.; Pasuk, I.; Ferreira, J.M.; Stan, G.E. Cationic substitutions in hydroxyapatite: Current status of the derived biofunctional effects and their in vitro interrogation methods. *Materials* **2018**, *11*, 2081. [[CrossRef](#)]
19. Ressler, A.; Žužić, A.; Ivanišević, I.; Kamboj, N.; Ivanković, H. Ionic substituted hydroxyapatite for bone regeneration applications: A Review. *Open Ceram.* **2021**, *6*, 100122. [[CrossRef](#)]
20. Kaneda, K.; Mizugaki, T. Development of concerto metal catalysts using apatite compounds for green organic syntheses. *Energy Environ. Sci.* **2009**, *2*, 655–673. [[CrossRef](#)]
21. Abukhadra, M.R.; Dardir, F.M.; Shaban, M.; Ahmed, E.A.; Soliman, M.F. Spongy Ni/Fe carbonate-fluorapatite catalyst for efficient conversion of cooking oil waste into biodiesel. *Environ. Chem. Lett.* **2018**, *16*, 665–670. [[CrossRef](#)]
22. Valizadeh, S.; Rasoulifard, M.H.; Dorraji, M.S. Modified Fe<sub>3</sub>O<sub>4</sub>-hydroxyapatite nanocomposites as heterogeneous catalysts in three UV, Vis and Fenton like degradation systems. *Appl. Surface Sci.* **2014**, *319*, 358–366. [[CrossRef](#)]
23. Moriguchi, T.; Sakamoto, Y.; Nakagawa, S. Heterogeneous photo-Fenton reaction of a herbicide atrazine by using Fe (III)-treated hydroxyapatites. *Phosphorus Res. Bull.* **2013**, *28*, 10–23. [[CrossRef](#)]
24. Campisi, S.; Galloni, M.; Marchetti, S.G.; Auroux, A.; Postole, G.; Gervasini, A. Functionalized Iron Hydroxyapatite as Eco-friendly Catalyst for NH<sub>3</sub>-SCR Reaction: Activity and Role of Iron Speciation on the Surface. *ChemCatChem* **2020**, *12*, 1676–1690. [[CrossRef](#)]
25. Galloni, M.G.; Campisi, S.; Marchetti, S.G.; Gervasini, A. Environmental Reactions of Air-Quality Protection on Eco-Friendly Iron-Based Catalysts. *Catalysts* **2020**, *10*, 1415. [[CrossRef](#)]
26. Gibert, O.; Valderrama, C.; Martínez, M.M.; Darbra, R.M.; Moncunill, J.O.; Martí, V. Hydroxyapatite Coatings on Calcite Powder for the Removal of Heavy Metals from Contaminated Water. *Water* **2021**, *13*, 1493. [[CrossRef](#)]
27. Goldberg, M.A.; Gafurov, M.R.; Murzakhanov, F.F.; Fomin, A.S.; Antonova, O.S.; Khairutdinova, D.R.; Pyataev, A.V.; Makshakova, O.N.; Konovalov, A.A.; Leonov, A.V.; et al. Mesoporous Iron (III)-Doped Hydroxyapatite Nanopowders Obtained via Iron Oxalate. *Nanomaterials* **2021**, *11*, 811. [[CrossRef](#)]

28. Goldberg, M.A.; Akopyan, A.V.; Gafurov, M.R.; Makshakova, O.N.; Donskaya, N.O.; Fomin, A.S.; Polikarpova, P.P.; Anisimov, A.V.; Murzakhanov, F.F.; Leonov, A.V.; et al. Iron-Doped Mesoporous Powders of Hydroxyapatite as Molybdenum-Impregnated Catalysts for Deep Oxidative Desulfurization of Model Fuel: Synthesis and Experimental and Theoretical Studies. *J. Phys. Chem. C* **2021**, *125*, 11604–11619. [[CrossRef](#)]
29. Ribeiro, T.P.; Monteiro, F.J.; Laranjeira, M.S. Duality of iron (III) doped nano hydroxyapatite in triple negative breast cancer monitoring and as a drug-free therapeutic agent. *Ceram. Int.* **2020**, *46*, 16590–16597. [[CrossRef](#)]
30. Laranjeira, M.S.; Moço, A.; Ferreira, J.; Coimbra, S.; Costa, E.; Santos-Silva, A.; Monteiro, F.J. Different hydroxyapatite magnetic nanoparticles for medical imaging: Its effects on hemostatic, hemolytic activity and cellular cytotoxicity. *Colloids Surfaces B Biointerfaces* **2016**, *146*, 363–374. [[CrossRef](#)]
31. Tampieri, A.; D'Alessandro, T.; Sandri, M.; Sprio, S.; Landi, E.; Bertinetti, L.; Panseri, S.; Pepponi, G.; Goettlicher, J.; Bañobre-López, M.; et al. Intrinsic magnetism and hyperthermia in bioactive Fe-doped hydroxyapatite. *Acta Biomater.* **2012**, *8*, 843–851. [[CrossRef](#)]
32. Gamal, G.A.; Al-Mufadi, F.A.; Said, A.H. Effect of iron additives on the microstructure of hydroxyapatite. *Eng. Technol. Appl. Sci. Res.* **2013**, *3*, 532–539. [[CrossRef](#)]
33. Sarath Chandra, V.; Baskar, G.; Suganthi, R.V.; Elayaraja, K.; Ahymah Joshy, M.I.; Sofi Beaula, W.; Mythili, R.; Venkatraman, G.; Narayana Kalkura, S. Blood Compatibility of Iron-Doped Nanosize Hydroxyapatite and Its Drug Release. *ACS Appl. Mater. Interfaces* **2012**, *4*, 1200–1210. [[CrossRef](#)]
34. Panseri, S.; Cunha, C.; D'Alessandro, T.; Sandri, M.; Giavaresi, G.; Marcacci, M.; Hung, C.T.; Tampieri, A. Intrinsically Superparamagnetic Fe-Hydroxyapatite Nanoparticles Positively Influence Osteoblast-like Cell Behaviour. *J. Nanobiotechnol.* **2012**, *10*, 1–10. [[CrossRef](#)] [[PubMed](#)]
35. Morrissey, R.; Rodriguez-Lorenzo, L.M.; Gross, K.A. Influence of ferrous iron incorporation on the structure of hydroxyapatite. *J. Mater. Sci. Mater. Med.* **2005**, *16*, 387–392. [[CrossRef](#)]
36. Nogueira, R.E.F.Q.; Graca, M.P.F.; Valente, M.A.; Sombra, A.S.B.; Silva, C.C. Structural and mechanical study of the sintering effect in hydroxyapatite doped with iron oxide. *Phys. B Condens. Matter* **2008**, *403*, 3826–3829.
37. Li, Y.; Nam, C.T.; Ooi, C.P. Iron (III) and manganese (II) substituted hydroxyapatite nanoparticles: Characterization and cytotoxicity analysis. *J. Phys. Conf. Ser.* **2009**, *187*, 012024. [[CrossRef](#)]
38. Vanderbilt, D. Soft self-consistent pseudopotentials in a generalized eigenvalue formalism. *Phys. Rev. B* **1990**, *41*, 7892. [[CrossRef](#)]
39. Giannozzi, P.; Baroni, S.; Bonini, N.; Calandra, M.; Car, R.; Cavazzoni, C.; Ceresoli, D.; Chiarotti, G.L.; Cococcioni, M.; Dabo, I.; et al. Quantum Espresso: A modular and open-source software project for quantum simulations of materials. *J. Phys. Condens. Matter* **2009**, *21*, 395502. [[CrossRef](#)] [[PubMed](#)]
40. Perdew, J.P.; Burke, K.; Ernzerhof, M. Generalized gradient approximation made simple. *Phys. Rev. Lett.* **1996**, *77*, 3865. [[CrossRef](#)]
41. Goldberg, M.; Gafurov, M.; Makshakova, O.; Smirnov, V.; Komlev, V.; Barinov, S.; Kudryavtsev, E.; Sergeeva, N.; Achmedova, S.; Mamin, G.; et al. Influence of Al on the structure and in vitro behavior of hydroxyapatite nanopowders. *J. Phys. Chem. B* **2019**, *123*, 9143–9154. [[CrossRef](#)]
42. Yashima, M.; Yonehara, Y.; Fujimori, H. Experimental visualization of chemical bonding and structural disorder in hydroxyapatite through charge and nuclear-density analysis. *J. Phys. Chem. C* **2011**, *115*, 25077–25087. [[CrossRef](#)]
43. Biktagirov, T.; Gafurov, M.; Mamin, G.; Klimashina, E.; Putlayev, V.; Orinskii, S. Combination of EPR measurements and DFT calculations to study nitrate impurities in the carbonated nanohydroxyapatite. *J. Phys. Chem. A* **2014**, *118*, 1519–1526. [[CrossRef](#)] [[PubMed](#)]
44. Monkhorst, H.J.; Pack, J.D. Special points for Brillouin-zone integrations. *Phys. Rev. B* **1976**, *13*, 5188–5192. [[CrossRef](#)]
45. Jiang, M.; Terra, J.; Rossi, A.M.; Morales, M.A.; Saitovitch, E.B.; Ellis, D.E. Fe<sup>2+</sup>/Fe<sup>3+</sup> substitution in hydroxyapatite: Theory and experiment. *Phys. Rev. B* **2002**, *66*, 224107. [[CrossRef](#)]